Capillary equilibrium of bubbles in porous media

Chuanxi Wang[a], Yashar Mehmani[b], and Ke Xu[a,1]

[a]Department of Energy and Resources Engineering, College of Engineering, Peking University, Beijing 100871, China; and [b]Department of Energy and Mineral Engineering, Pennsylvania State University, University Park, PA16802

Edited by David A. Weitz, Harvard University, Cambridge, MA, and approved March 21, 2021 (received for review November 25, 2020)

In geologic, biologic, and engineering porous media, bubbles (or droplets, ganglia) emerge in the aftermath of flow, phase change, or chemical reactions, where capillary equilibrium of bubbles significantly impacts the hydraulic, transport, and reactive processes. There has previously been great progress in general understanding of capillarity in porous media, but specific investigation into bubbles is lacking. Here, we propose a conceptual model of a bubble's capillary equilibrium associated with free energy inside a porous medium. We quantify the multistability and hysteretic behaviors of a bubble induced by multiple state variables and study the impacts of pore geometry and wettability. Surprisingly, our model provides a compact explanation of counterintuitive observations that bubble populations within porous media can be thermodynamically stable despite their large specific area by analyzing the relationship between free energy and bubble volume. This work provides a perspective for understanding dispersed fluids in porous media that is relevant to CO_2 sequestration, petroleum recovery, and fuel cells, among other applications.

bubble | porous media | capillary pressure | hysteresis | surface free energy

Bubbles are generated, trapped, and mobilized within porous media as a consequence of incomplete fluid–fluid displacements (1, 2), phase changes (3, 4), chemical and biochemical reactions (5, 6), or injection of emulsified fluids and foams (7, 8). Compared to continuously connected phases, the behavior of dispersed bubbles, or ganglia, are far less understood. In particular, the thermodynamic stability of bubbles, despite their large specific surface area, remains a puzzle. The difficulty comes from the fact that each bubble can attain a volume (V), topology, and capillary pressure (P_c) that is distinct from other bubbles in the medium (9). The variability poses challenges to understanding the transport and trapping mechanisms of bubbles in geologic CO_2 sequestration (10, 11), hydrocarbon recovery (12, 13), fuel cell water management (14, 15), and vadose zone oxygen supply (16, 17).

The dominant factor controlling a bubble's behavior in a porous medium is capillarity, which is typically much larger than either viscous, gravitational, or inertial forces (18, 19). Capillary pressure, P_c, allows a closure relationship for two-phase Darcy Eqs. (20–22) and influences thermodynamic properties like phase partition (23). Capillary pressure is derived from the Young–Laplace equation $P_c = \gamma\kappa$, where γ is the interfacial tension and κ is the surface curvature. In an open space without obstacles, a bubble spontaneously evolves into a sphere to minimize its total interfacial energy. Thus, P_c is a continuous and monotonically decreasing function of V (Fig. 1*A*). However, in a porous medium, bubble's P_c–V relation is more complicated due to the geometric confinement imposed by the porous structure and topological evolution (24). A bubble can no longer remain spherical as it grows in size but must conform to the geometry of the pore(s) it occupies. Therefore, a bubble's P_c is a function of not only its volume and interfacial tension but also its topology as dictated by the confining porous medium, as confirmed by recent laboratory experiments and numerical simulations (25–29). The mere presence of confinement therefore engenders a host of phenomena that would otherwise be absent, such as capillary trapping (30, 31), anticoarsening of bubble populations (32, 33), and complex ganglion dynamics (11, 18). Furthermore, theoretical studies in mathematical topology (28, 34, 35) prove that immiscible fluids can be fully characterized by $d+1$ Minkowski functionals, where d is the problem dimension. Such characterizations remove the path-dependent (or hysteretic) behavior common to these systems (34, 35).

Recent developments in microfluidics and micro computed tomography imaging allow detailed pore-scale visualizations of fluids inside porous media, including the morphology of bubbles and ganglia (25, 36–39). Garing et al. (25) experimentally measured the equilibrium capillary pressure of trapped air bubbles inside sandstone and bead-pack samples. They found that, unlike bubbles within a bulk fluid, the P_c of trapped bubbles shows no clear dependence on V and seems to fall within a bounded interval, except for vanishingly small V. Xu et al. (40) proposed an empirical correlation for the P_c trapped bubbles based on microfluidic observations. In this correlation, as V increases, P_c decreases until a minimum is reached and then increases linearly. In the first stage, the bubble is unconfined, whereas in the second, it is reshaped by the surrounding solid walls. The proposed correlation, however, is only valid for bubbles in a single pore and not bubbles that span multiple pores. The latter seems to be rather common in nature as evidenced by recent direct observations (Fig. 1*B*) (2, 25).

Here, we propose a simple conceptual model to describe the equilibrium states of a bubble with arbitrary size trapped inside a porous medium. The model accounts for the bubble's morphology, the geometry of the solid matrix, and the wettability between the two. We derive all metastable configurations of the bubble analytically and highlight the thermodynamic states the bubble assumes when it is static, growing, or shrinking. We also show that the relationship between surface free energy (F) and volume

Significance

We show how pore geometry modulates the capillary equilibrium states of a trapped bubble inside a porous medium using a simple conceptual model. The model explains recently published data on bubbles trapped in porous rock samples. We explain the counterintuitive observation that bubbles with large surface areas in the subsurface can remain thermodynamically stable for geologically long times. The stability is the result of a modified relationship between a bubble's surface free energy and volume due to geometric confinement. The implications are relevant to applications ranging from petroleum recovery, to CO_2 sequestration, to groundwater oxygen supply, and to fuel-cell water management.

Author contributions: K.X. designed research; C.W. performed research; Y.M. contributed new reagents/analytic tools; C.W. and K.X. analyzed data; and C.W., Y.M., and K.X. wrote the paper.

The authors declare no competing interest.

This article is a PNAS Direct Submission.

[1]To whom correspondence may be addressed. Email: kexu1989@pku.edu.cn.

This article contains supporting information online at https://www.pnas.org/lookup/suppl/doi:10.1073/pnas.2024069118/-/DCSupplemental.

Published April 19, 2021.

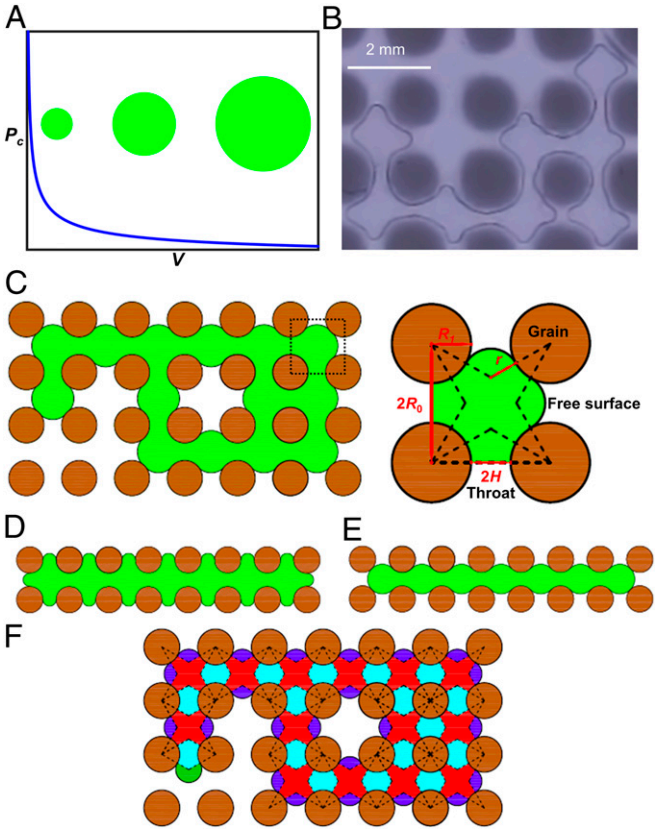

Fig. 1. (*A*) Spherical bubbles inside a bulk fluid. (*B*) Micromodel observations show that bubbles are nonspherical in porous media and may occupy multiple pores. This image is from *SI Appendix*, Movie S1. (*C*) A 2D porous medium comprised of an ordered array of identical circular grains. A bubble occupying multiple pores including a zoom-in to a portion of it. (*D*) Illustration of the full state. (*E*) Illustration of the critical state. (*F*) Decomposition of a bubble into four distinct parts: minor arc menisci shown by dark blue cap-shaped regions, throats shown by light blue diamond-shaped regions, inner bulk bodies shown by red star-shaped regions, and major arc menisci shown by dark green cap-shaped regions.

(V) of large bubbles is approximately linear, which explains the previously counterintuitive observation that such bubbles are thermodynamically stable despite having large surface areas. Our work provides a step toward understanding the capillary state, stability, and evolution of dispersed immiscible fluids in porous media.

Conceptual Model

Consider a static bubble inside a two-dimensional (2D) porous medium consisting of a rectangular array of identical circular grains (Fig. 1*C*). The bubble is assumed to be perfectly nonwetting (i.e., contact angle is $\theta = 0$). The impact of noncircular grain shapes and nonzero contact angles will be discussed later. We call the void space enclosed between four adjacent grains a pore and the narrow constriction that connects two neighboring pores a throat. The bubble can reside either within one pore or multiple pores. The number of pores occupied by the bubble is referred to as its pore occupancy, n. When $n > 1$, the bubble may have multiple branches that meander and occupy pores in different directions. Moreover, the branches can self-intersect, leaving isolated islands of the wetting phase stranded in the middle (Fig. 1*F*). To quantify the topology of the bubble, we use the Euler characteristic, χ (30, 41). The Euler characteristic is defined as $\chi = \beta_0 - \beta_1 + \beta_2$, where β_i are called Betti numbers (26, 28). β_0 denotes the number of disconnected objects, β_1 the number of redundant loops, and β_2 the number of cavities in the object. Because we only analyze one bubble at a time in this work, $\beta_0 = 1$, and because we focus on 2D, $\beta_2 = 0$. The only Betti number of relevance to us is therefore β_1, which is proportional to the number of self-intersections of the bubble's branches (i.e., each intersection creates a new hole). In *SI Appendix*, SI.3.2, we provide a detailed analysis that shows χ and n are constrained by the following interval: $2\sqrt{n} - n \leq \chi \leq 1$.

In a 2D porous medium, three functionals are needed to be specified in order to constrain the thermodynamic state of a bubble (28, 35). Recent studies (29) show the hysteresis of immiscible two-fluid systems to be an artifact of omitting one of these functionals. Here, we choose V, n, and χ as the three parameters to describe equilibrium states of a bubble, which are related (as we shall see) to the aforementioned Minkowski functionals.

Geometric parameters relevant to our study are annotated in Fig. 1*C*. We denote the radius of the grains by R_1, the half-distance between the centers of two adjacent grains by R_0 and the half-width of the throats by H. The volume (i.e., area in a 2D system) of a pore is denoted by V_{pore} and its area (i.e., or perimeter in 2D) by A_{pore}. We assume a free surface is constrained by two neighboring solid grains for simplicity.

We assume that the bubble is in static equilibrium and that no external fields are imposed. The 2D bubble's free surface (not touching the grain surfaces) has therefore a uniform interfacial curvature denoted by $\kappa = 1/r$, where r is the radius of curvature. Since snap-off events can't happen in our 2D (42, 43), the bubble is assumed to remain as one connected piece as it evolves in size, which simplifies our analysis. To analyze and determine the thermodynamic state of the bubble, we divide it into four distinct element types as shown by Fig. 1*F*. Calculations related to each element type are provided in *Methods*.

We next describe the capillary pressure (P_c) and surface (or Helmholtz) free energy (F) of the bubble for all metastable states it can assume. The mathematical details for calculating P_c and F are provided in *Methods*. Here, we simplify the discussion by introducing the following terminology that correspond to two important bubble states:

- The full state refers to when the bubble attains the maximum volume it can sustain at a given pore occupancy n and Euler characteristic χ (Fig. 1*D*). The capillary pressure associated with the full state is the capillary entry pressure of the throats, $P_{c,\ throat}$.
- The critical state refers to when the bubble attains the minimum capillary pressure it can sustain at a given n and χ (Fig. 1*E*). The capillary pressure associated with the critical state is denoted by $P_{c,\ min}$, which corresponds to the capillary pressure of the maximum inscribed sphere of a pore.

In the following, we repeatedly refer to the static bubble as "trapped" even though its size may grow or shrink due to ripening or other mass transfer processes. The term "trapped" here means "static" and "in capillary equilibrium." We shall use the two terms interchangeably.

Results and Discussion

In this section, we first analyze the equilibrium states of a trapped bubble through a series of demonstrative examples. We then focus on the bubble's surface free energy and show how it depends on the bubble's volume and morphology. Implications for the stability of dispersed bubble populations are highlighted. We finally generalize our discussion by considering different grain shapes, pore-throat aspect ratios, and contact angles. In all subsequent figures, $R_0/H = 6$, which is representative of previous micromodel experiments (33).

Bubble Multistability. In *SI Appendix*, SI.1, we derive a closed-form equation for P_c (and F) as a function of V, n, and χ. The model shows that for a bubble of fixed V, multiple metastable states corresponding to different (n, χ) pairs exist. Since n and χ are integers, the P_c equation depicted by Fig. 2*A* is a piecewise continuous function that consists of many disconnected segments. Each segment corresponds to a different (n, χ) pair, for which $P_c = \partial F/\partial V$ holds. The discontinuous and highly oscillatory dependence of P_c on V, n, and χ highlights the need for a different approach to describing the capillary equilibrium of trapped bubbles than the one provided by existing Darcy-scale theories of two-phase flow, which treat nonwetting fluids as continuously connected phases.

For $n = 1$, it is easy to verify that $\chi = 1$. This corresponds to the first segment of P_c-V in Fig. 2*A*, which decreases from infinity at very small V to a minimum $P_{c,\ min}$, followed by an increase toward $P_{c,\ throat}$. For $n > 1$, all P_c-V segments are bounded within the interval $[P_{c,\ min}, P_{c,\ throat}]$ regardless of n or χ. The result is consistent with previous laboratory experiments in homogeneous bead packs (25). There, the authors found that the P_c of trapped bubbles fall within a narrow interval, where the correlation to V is weak except at very small V.

Fig. 2*B* shows the P_c-V segments associated with $\chi = 1$ but different values of n. Fig. 2*C* shows the P_c-V segments associated with $n = 24$ and all possible values of χ. Here, P_c changes more rapidly with V for smaller values of χ (i.e., corresponding to more self-intersections). We also note that the number of metastable states increases with V, as shown by Fig. 2 *A* and *B*.

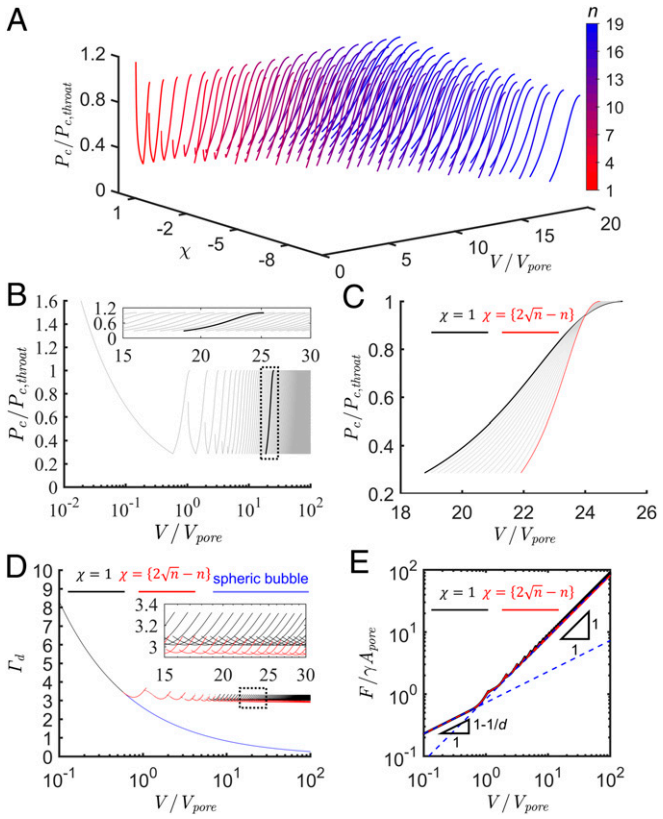

Fig. 2. Relationship between P_c, V, A, n, and χ for $R_0/H = 6$ in an ordered array of circular grains. (*A*) A schematic of the relation $P_c = f(V, n, \chi)$. Each segment corresponds to a different (n, χ) pair, stretching along the P_c-V plane. Larger V entails larger n and thus a higher possibility of self-intersection leading to more negative χ. (*B*) A projection of $P_c = f(V, n, \chi = 1)$ on the P_c-V plane and V axis is in log scale. The *Inset* is a zoom-in at large V. The solid black curve corresponds to $n = 24$, and the solid gray curves correspond to other values of n. (*C*) A projection of $P_c = f(V, n = 24, \chi)$ on the P_c-V plane. More negative χ corresponds to steeper P_c-V curve segments. In *C*, *D*, and *E*, the solid black curve indicates the maximum $\chi = 1$ and the solid red curve the minimum $\chi = \{2\sqrt{n} - n\}$. (*D*) Dimensionless specific interfacial area (Γ_d) versus dimensionless bubble volume. The solid blue curve corresponds to a spherical bubble in open space. The *Inset* is a zoom-in at large V. (*E*) Relation between dimensionless total surface area and dimensionless bubble volume. At large V, the area A is proportional to V, while at small V, A is proportional to $V^{1-1/d}$. d is the problem dimension (=2 here). The dotted blue lines correspond to the slope 1−1/d and 1.

Surface Free Energy and Bubble Population Stability. Here, we analyze the thermodynamic stability of a population of trapped bubbles by considering their surface free energy (F) under isothermal conditions and no external fields (9). Much like P_c, F is also a function of V, n, and χ in 2D porous media. We choose the reference energy as that of a fully saturated wetting phase without any bubbles, to which we assign the value zero.

The stability of a population of isolated bubbles is governed by the specific relation between F and V. Assuming $F \propto V^m$ holds for each bubble, let us define the following ratio:

$$\frac{F_{connnected}}{F_{isolated}} = \frac{(\sum V_i)^m}{(\sum V_i^m)} \begin{cases} <1, & if\ m<1 \\ =1, & if\ m=1 \\ >1, & if\ m>1 \end{cases}, \qquad [1]$$

where V_i is the volume of each isolated bubble. $F_{isolated}$ denotes the collective free energy of all the isolated bubbles, whereas $F_{connected}$ denotes the free energy of a hypothetical bubble that has a volume equal to the sum of the volumes of all the isolated bubbles. We see that when the exponent m <1, it is energetically favorable for the bubbles to coalesce into one because the free energy is then lower. This is the case with spherical bubbles in the absence of confinement, where $m = 1-1/d$ such that d is the problem dimension. Such a sublinear F-V scaling is indeed the driving force behind classical Ostwald ripening in bulk fluids that coarsens the bubble population (44).

However, the validity of the above argument for a bubble confined inside a porous medium was heretofore unknown. To address this gap, we examine the dependence of F upon V, n, and χ. Notice first that $F = \gamma A = \gamma \Gamma V$, where A is the total area of the bubble and $\Gamma = A/V$ is its specific surface area. In *SI Appendix*, SI. 1.8, we derive closed-form expressions for F and Γ as functions of V, n, and χ. In Fig. 2*D*, we plot $\Gamma_d = R_0 A/V$ (dimensionless Γ) versus V/V_{pore} (dimensionless volume) for all possible values of n. Only graphs corresponding to the maximum (black) and minimum (red) values of χ, at each V and n, are shown. The graphs correspond to the black and red lines in Fig. 2*C*. We see that for very small V, Γ_d is identical to that of an unconfined spherical bubble (blue line). But as V increases further, Γ_d starts to fluctuate within a bounded interval. This interval is analytically derived and given below:

$$\Gamma_d \in 2\pi \cdot \left[\frac{1}{4R_0/R_1 - \pi R_1/R_0},\ \frac{1}{4 + \pi - 2\pi R_1/R_0} \right]. \qquad [2]$$

The upper bound of this interval corresponds to the full state of a bubble at maximal χ =1, whereas the lower bound corresponds to a state with $d\Gamma/dV = 0$ (not the same as critical state) at minimal $\chi = 2\sqrt{n} - n$. The interval shrinks for smaller values of porosity ($\varphi = 1 - \pi R_1^2/4R_0^2$).

In geologic porous media, $R_0/R_1 < 2$ (corresponding to φ<0.8) typically holds (45–47). As a result, the interval in Eq. **2** for Γ_d is $2\pi \cdot [0.16,\ 0.25]$. This implies a nearly constant specific surface area at large bubble volumes, which is in agreement with previous experimental observations in homogenous rock samples (Fig. 14 in ref. 39 and Fig. 6 in ref. 48). Since $\Gamma = A/V$ is almost

constant, the relation between $A = \Gamma V$ and V (for $n > 1$) must be approximately linear as shown by Fig. 2*E*. Therefore, $m \sim 1$ in Eq. **1**, also in agreement with published data (2, 49–51). Notice that n and χ play a relatively minor role in the calculated value of Γ and thus F. This is similar to the findings of ref. 29, where some of the geometric state variables of two-fluid systems can be dependent on one another provided a minor error can be tolerated.

The linearity of *F-V* implies that the coalescence of confined bubbles is energetically less favorable ($m \sim 1$) than free bubbles in a bulk fluid ($m < 1$). Coalescence, therefore, does not necessarily reduce F except at vanishingly small and spherical bubble volumes ($F \propto V^{1-1/d}$). This explains why trapped bubble populations are frequently found within geologic porous media. Despite their large Γ, the bubbles have no affinity to merge and can remain stable over geologic time scales. Now the kinetics of bubble coarsening, or the time needed to reach equilibrium, is a separate but important issue that the authors we will explore in the future.

Capillary Hysteresis during Bubble Growth–Shrinkage. Bubble growth and shrinkage often accompany physical and chemical processes such as phase change, degas/dissolution, gas-generating/consuming chemical/biochemical reactions, and volumetric expansion due to pressure and temperature changes. Here, we track the changes in bubble morphology, P_c, and F during a growth–shrinkage cycle (Fig. 3*A*). We show that the process is hysteretic because of the multistability of trapped bubbles in porous media.

Theoretical tools in mathematical topology, such as Minkowski functionals, provide an elegant framework with which to analyze and understand hysteresis of general immiscible multiphase fluid systems (35). Here, we use conceptually simpler tools to examine hysteresis during growth–shrinkage cycles so as to appeal to the physical intuition of the process. For simplicity, we take $\chi = 1$, although a similar analysis holds for other values of χ.

Consider a bubble that grows from an initial volume $V = 0$. With reference to the blue arrows in Fig. 3*A*, the following stages govern growth:

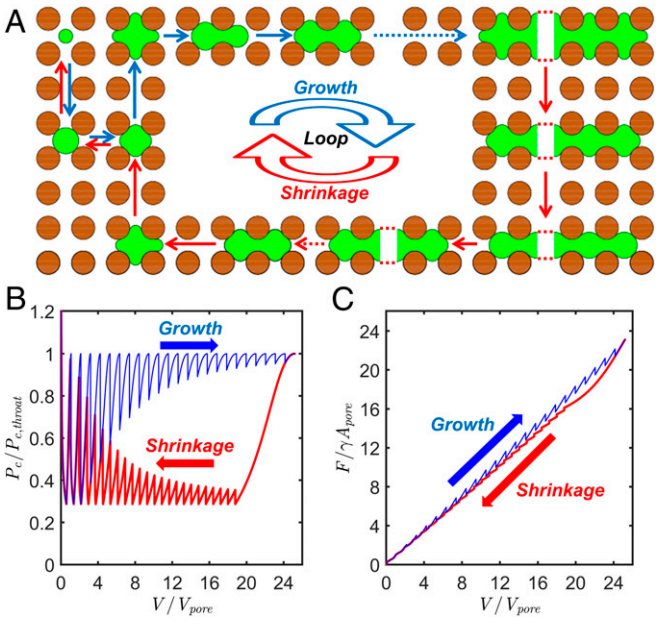

Fig. 3. (*A*) A growth and shrinkage loop of a bubble. Blue arrows show a bubble growing from small V with $n = 1$, while red arrows show a bubble shrinking from large V. (*B* and *C*) The nonmonotonic and discontinuous P_c-V and *F-V* paths of growth and shrinkage. Blue corresponds to growth and red to shrinkage. $R_0/H = 6$ and the domain is a circular disk pack.

- Free growth (*FG*) is the period when the bubble is too small to be constricted by the pore geometry. P_c gradually decreases with V in a manner identical to a spherical bubble free from any solid constraints.
- Constricted growth (*CG*) starts when the bubble has grown sufficiently large to have touched the four confining grains, as the solid blue bubble in Fig. 1*E* illustrates. Further growth in V leads to the distortion of the bubble surface to conform to the pore geometry. In *CG*, P_c increases gradually until the full state is reached, where $P_c = P_{c,throat}$.
- Breakthrough event (*BT*) occurs right after the bubble reaches the full state. Any further increase in V causes the penetration of one of the end-point menisci through a throat. The entire configuration of the bubble becomes unstable, and a sudden redistribution of mass ensues. *BT* is manifested by a sudden jump in P_c -V from one curve segment to the next. During a *BT*, P_c drops from $P_{c,\ throat}$ to a lower value, and n increases by one (Fig. 1*E*).
- Further increase in V leads to a repetition of *CG* and *BT* stages. As a result, the P_c-V appears to fluctuate up and down.

We next track a bubble that shrinks from an initially large V and n. With reference to the green and red arrows in Fig. 3*A*, the following stages govern shrinkage:

- Constricted shrinkage (*CS*) is the period when the bubble shrinks without detaching from any of the surrounding grains, as the solid blue bubble in Fig. 1*F* illustrates. If the bubble is initially at the full state, P_c gradually decreases from $P_{c,\ throat}$ with all the menisci retracting simultaneously and maintaining a uniform curvature.
- Flinch event (*FC*) occurs right after the bubble reaches the critical state. Any further decrease in V leads to an unstable configuration that cannot be sustained by the current n. Hence, the bubble retracts inward to rearrange its shape. The result of *FC* is a sudden surge in P_c and a decrease in n by one (Fig. 1*F*).
- Further decrease in V leads to a repetition of *CS* and *FC* stages. As a result, the P_c-V relation appears to fluctuate up and down while bounded below by $P_{c,\ min}$.
- Free shrinkage (*FS*) is the period when the bubble has reduced sufficiently in size to occupy a single pore without touching any of the surrounding grains. The P_c-V relation overlaps with that of free growth (*FG*).

Fig. 3*B* shows that the above growth–shrinkage cycle exhibits by a sawtooth P_c-V path. The growth route traces the maximum possible P_c at any given V, while the shrinkage path the minimum possible P_c at any given V. The two paths, therefore, are completely different and show significant hysteresis. The *F-V* paths corresponding to the above growth–shrinkage cycle are also shown in Fig. 3*C*, which similarly exhibit hysteresis.

The *FG*, *CG*, *CS*, and *FS* periods are all reversible. The only sources of irreversibility, and thus hysteresis, are *BT* and *FC* events that dissipate energy by rapid reconfiguration. The two events are very similar to the classical pore-scale irreversible processes that govern fluid–fluid displacements in porous media: Haines jumps (rheons) and Melrose events (9, 52, 53). *BT* and *FC* events lead to the adjustment of the bubble interfaces in every occupied pore. For example, a *BT* results in not only the interface advancing in the newly invaded pore but also simultaneous interface recoiling in all previously occupied pores as compensation to keep bubble volume conservative. *SI Appendix*, Movie S1 visualizes *BT* events in a micromodel experiment where a bubble grows due to slow depressurization. We note that recent works in mathematical topology provide a promising means of characterizing the observed hysteresis herein with a unique state function (see Discussions under the "ink bottle problem" therein) (27). This pore-scale picture of bubble capillary hysteresis is aligned

with classical pictures for fluid–fluid displacement hysteresis at pore scale (9, 24) and mesoscale (54).

As shown by Fig. 3*B*, the oscillations in P_c attenuate as V increases and disappear altogether at the limit $V \to \infty$. At large V, the growth path asymptotes to $P_{c,\ throat}$ and the shrinkage path to $P_{c,\ min}$. More importantly, discontinuities in both paths gradually disappear, and the P_c-V curves become continuous. Since an infinitely large bubble is essentially a continuous phase, we see indications that both P_c-V paths seem to approximate drainage/imbibition P_c-S curves (where S is saturation) used in classical Darcy-scale theories of fluid displacement. An exact characterization of these limits, however, requires additional tools outside the scope of this paper. Recent advances in mathematical topology (29) provide a promising avenue.

Impacts of Geometry and Wettability. To determine the generality of the results discussed thus far, we examine the qualitative impacts of grain shape, throat-to-grain ratio, and contact angle ($<\pi/2$) on the equilibrium states of a trapped bubble.

In *SI Appendix*, SI.4, we show that none of the geometric factors or wettability qualitatively alter our previous conclusions about the multistability of bubbles, linear scaling between free energy and volume, and hysteresis during growth–shrinkage cycles, at least for the parameter ranges considered. They do, however, have an important quantitative impact on, for example, the amplitude and wavelength of P_c-V and F-V oscillations. More specifically, larger throat-to-grain ratios result in weaker fluctuations of P_c and F; different grain shapes change each P_c-V segment quantitatively; and nonzero contact angles sometimes lead to negative $P_{c,\ min}$.

Implications and Limitations. Our conceptual model is distinct from classical capillary pressure models at the Darcy scale. The latter assume that each phase is hydrodynamically connected throughout the sample (13, 19) and that fluid–fluid interfaces are always at capillary equilibrium. However, bubbles are disconnected entities with possibly different thermodynamic states.

Our conceptual model is admittedly limited by several assumptions. These include the following: 1) the roles of heterogeneity and polydispersity in pore sizes are neglected that will likely have significant impact on bubble growth, shrinkage, and hysteresis (54, 55); 2) All external fields such as gravity, background flow, and concentration gradients are neglected. The last item can induce Marangoni effects at the bubble surface driving the system away from the metastable states discussed herein and toward new ones (56); 3) The model does not apply to very tight packings of bubbles, like foams, as that requires keeping track of the separating lamella that delineate the boundary of each bubble; and 4) Perhaps most importantly, our model is 2D. In three-dimensional (3D), interfaces consist of two principle curvatures, with possibly opposite signs (i.e., be saddle points) (57) that may lead to new metastable states. The reason for this assumption was that closed-form expressions seemed possible, at least to us, only in 2D but immensely difficult in 3D. While no conclusive claims can yet be made about capillary equilibria of 3D bubbles, we suspect the qualitative observations made herein remain intact. A quantitatively rigorous analysis in 3D is possible with computational techniques such as level set (58, 59) and lattice Boltzmann (60–62) methods, which pose an obvious next step for future analysis.

Conclusion

We developed a 2D conceptual model that describes the equilibrium capillary pressure (P_c) and surface free energy (F) of a static bubble trapped inside a porous medium. Closed-form equations are derived for both quantities as functions of bubble volume V, pore occupancy n, and Euler characteristic χ. The conceptual model revealed that bubbles have fundamentally different capillary properties than those in a bulk fluid.

For a 2D ordered disk pack, a typical P_c-V curve consists of many piecewise continuous segments, each of which corresponding to a different (n, χ) pair. For $n > 1$, all segments fall within the interval $[P_{c,\ min}, P_{c,\ throat}]$, which itself depends on the pore geometry. The free energy (or specific surface area) of the bubble falls, surprisingly, within a similar but narrower interval. The implication is an approximately linear relationship between F and V. The linearity means that the merger of isolated bubbles is not necessarily favorable energetically, which explains the thermodynamic stability of large ganglia observed in a geologic porous media. This model explains the observations from many previous experimental observations (25–28, 33, 39, 48)

We also compute P_c and F during a growth–shrinkage cycle of a trapped bubble and find that both quantities are highly oscillatory and discontinuous functions of V. Moreover, the growth and shrinkage paths do not overlap. The hysteresis is attributed to energy dissipations during sudden and thus irreversible breakthrough and flinch events following changes in pore occupancy. The oscillations in both P_c and F disappear as V approaches infinity, indicating some sort of "convergence" toward a macroscopic state.

Though our model is simple, we believe that it serves as a useful entry point toward predictive macroscopic theories of bubble mobilization, trapping, and ripening in porous media. Such theories are needed to answer important questions related to hydrocarbon migration, gas-hydrate formation, CO_2 sequestration, and fuel-cell design.

Methods

Correlate P_c to V, n, and χ. We divide the bubble into four distinct element types as shown in Fig. 1*F*: (a) minor arc menisci of volume V_{minor}, (b) throats of volume V_{throat}, (c) inner regions of the pore-body of volume V_{body}, and (d) major arc menisci of volume V_{major}. The V_{minor}, V_{throat}, V_{body}, and V_{major} are all functions of the free surface curvature radius, r, for a given matrix geometry and wettability. The total volume of the bubble can thus be written as

$$V = n_1 \cdot V_{minor}(r) + n_2 \cdot V_{throat}(r) + n_3 \cdot V_{body}(r) + n_4 \cdot V_{major}(r), \quad [3]$$

where n_i denotes the total number of each element in the bubble. To obtain n_i, we solve the following system of equations, formulated by imposing a set of morphological constraints:

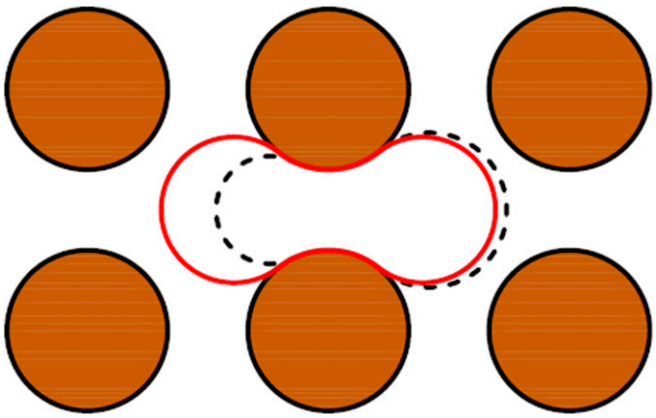

Fig. 4. An example of a bubble with an unstable morphology. The solid red line is the bubble at equilibrium before perturbation, while the black dashed line is the bubble after perturbation. Th perturbation amplifies while V remains unchanged.

$$\begin{cases} 4n_3 = n_1 + 2n_2 - n_4 \\ n_3 + n_4 = n \\ n_3 + n_4 - n_2 = \chi \end{cases}. \quad [4]$$

Expressions for n_i, V_i, and A_i are derived in *SI Appendix*, SI.1. The first row of Eq. **4** can be interpreted as an accounting of all the pores' open faces occupied by the bubble. The second row of Eq. **4** defines the pore occupancy, n. The third row defines the Euler characteristic, χ (30, 41). We note that, as long as $0 \le n_4 \le \min\{n, 2(n+\chi)/3\}$, there could be multiple solutions to Eq. **4**. While all solutions ensure the bubble is at equilibrium (i.e., all interfaces share the same curvature), they do not necessarily represent metastable states. At a metastable state, the morphology of a bubble should spontaneously recover from an infinitely small perturbation of the bubble's position. By contrast, a bubble that is not at a metastable state will amplify the tinniest of perturbations until the bubble finds a metastable state. See Fig. 4, for example. After a small perturbation, the solid red bubble will change to the dashed black bubble and become unstable. We therefore need more constraints to exclude unstable configurations.

Details of the analysis of metastable bubble morphology are given in *SI Appendix*, SI.2. The conclusion is that n_4 can only be 0 or 1. Specifically, when $n_4 = 0$, the bubble is always stable and $\partial V/\partial r < 0$ holds, but when $n_4 = 1$, the bubble is stable only when $\partial V/\partial r > 0$. This criterion is derived from general physical principles and is valid regardless of grain shape, contact angle, and dimension. In short, the constraint to ensure metastability is as follows:

$$n_4 = 0 \cup \{1 \cap \partial V/\partial r > 0\}. \quad [5]$$

In (*SI Appendix*, SI.4.2), we derive explicit expressions for $V_{minor}(r)$, $V_{throat}(r)$, $V_{body}(r)$, and $V_{major}(r)$ for different grain shapes and wettability. Combined with Eqs. **3**–**5** and the mathematical derivation in *SI Appendix*, SI.3.1, we are able to obtain a closed-form equation for $r = f(V, n, \chi)$. P_c is then readily obtained via $P_c = \gamma/r$. Because r is a function of V, n, and χ, so is P_c.

***F* versus *V*, *n*, and χ.** For a given n and χ, $dF/dV = P_c$ (9). Since P_c is a function of V, n, and χ obtained from the previous section, F can also be written as a function of V, n, and χ. We set the reference free energy as that of a fully saturated liquid with no bubbles.

To determine F of a static equilibrated bubble, we also look into the four distinct element types as shown in Fig. 1*F* and denote the surface area of 1) minor arc menisci of surface area A_{minor}, 2) throats of surface area A_{throat}, 3) inner regions of the pore-body of surface area A_{body}, and 4) major arc menisci of surface area A_{major}. The A_{minor}, A_{throat}, A_{body}, and A_{major} are all functions of r for a given matrix geometry and wettability. The total surface area of the bubble can thus be written as the following:

$$F = n_1 \cdot \gamma_1 A_{minor}(r) + n_2 \cdot \gamma_2 A_{throat}(r) + n_3 \cdot \gamma_2 A_{body}(r) + n_4 \cdot \gamma_1 A_{major}(r), \quad [6]$$

where γ_1 is the interfacial tension at the free surface and γ_2 is the interfacial tension at a constrained surface. For a completely nonwetting bubble, $\gamma_1 = \gamma_2 = \gamma_{gl}$; for a nonzero contact angle ($=\theta$) case, $\gamma_1 = \gamma_{gl}$, and $\gamma_2 = \gamma_{gs} - \gamma_{ls} = \gamma_{gl}\cos\theta$ is the difference between solid–gas interfacial tension and solid–liquid interfacial tension. In *SI Appendix*, SI.4.2, we derive explicit expressions for $A_{minor}(r)$, $A_{throat}(r)$, $A_{body}(r)$, and $A_{major}(r)$ for different grain shapes and wettability. We then obtain a functional form of $F = g(V, n, \chi)$.

Data Availability. All study data are included in the article and/or supporting information.

ACKNOWLEDGMENTS. We gratefully acknowledge support and funding from CNPC Research Institute of Petroleum Exploration and Development for the project "Key Fluid Mechanisms of CO2-EOR for Gu-Long Shale Oil Development," and from Beijing Innovation Center for Engineering Science and Advanced Technology at Peking University. We also benefited a lot from helpful discussions with Dr. Ruben Juanes at Massachusetts Institute of Technology and Dr. Jinhan Xie and Dr. Sheng Mao at Peking University. Movie S1 was captured by Dr. Yandong Zhang in Xu's research group.

1. A. Mehmani, S. Kelly, C. Torres-Verdín, M. Balhoff, Capillary trapping following imbibition in porous media: Microfluidic quantification of the impact of pore-scale surface roughness. *Water Resour. Res.* **55**, 9905–9925 (2019).
2. H. Geistlinger, I. Ataei-Dadavi, S. Mohammadian, H. J. Vogel, The impact of pore structure and surface roughness on capillary trapping for 2-D and 3-D porous media: Comparison with percolation theory. *Water Resour. Res.* **51**, 9094–9111 (2015).
3. W. Ehlers, K. Häberle, Interfacial mass transfer during gas–liquid phase change in deformable porous media with heat transfer. *Transp. Porous Media* **114**, 525–556 (2016).
4. Y. C. Yortsos, A. K. Stubos, Phase change in porous media. *Curr. Opin. Colloid Interface Sci.* **6**, 208–216 (2001).
5. J. J. Lay, T. Miyahara, T. Noike, Methane release rate and methanogenic bacterial populations in lake sediments. *Water Res.* **30**, 901–908 (2014).
6. K. Wang *et al*., Growth of oxygen bubbles during recharge process in zinc-air battery. *J. Power Sources* **296**, 40–45 (2015).
7. K. D. Danov, D. S. Valkovska, P. A. Kralchevsky, Hydrodynamic instability and coalescence in trains of emulsion drops or gas bubbles moving through a narrow capillary. *J. Colloid Interface Sci.* **267**, 243–258 (2003).
8. B. Géraud, S. A. Jones, I. Cantat, B. Dollet, Y. Méheust, The flow of a foam in a two-dimensional porous medium. *Water Resour. Res.* **52**, 773–790 (2016).
9. N. R. Morrow, Physics and thermodynamics of capillary action in porous media. *Ind. Eng. Chem.* **62**, 32–56 (1970).
10. R. Juanes, E. J. Spiteri, F. M. Orr, M. J. Blunt, Impact of relative permeability hysteresis on geological CO2storage. *Water Resour. Res.* **42** (2006).
11. H. E. Huppert, J. A. Neufeld, The fluid mechanics of carbon dioxide sequestration. *Annu. Rev. Fluid Mech.* **46**, 255–272 (2014).
12. T. Lee, L. Bocquet, B. Coasne, Activated desorption at heterogeneous interfaces and long-time kinetics of hydrocarbon recovery from nanoporous media. *Nat. Commun.* **7**, 11890 (2016).
13. L. W. Lake, R. T. Johns, W. R. Rossen, G. A. Pope, *Fundamentals of Enhanced Oil Recovery* (Society of Petroleum Engineers, Richardson, TX, ed. 2, 2014).
14. M. Andersson, S. B. Beale, M. Espinoza, Z. Wu, W. Lehnert, A review of cell-scale multiphase flow modeling, including water management, in polymer electrolyte fuel cells. *Appl. Energy* **180**, 757–778 (2016).
15. Z. Lu, M. M. Daino, C. Rath, S. G. Kandlikar, Water management studies in PEM fuel cells, part III: Dynamic breakthrough and intermittent drainage characteristics from GDLs with and without MPLs. *Int. J. Hydrogen Energy* **35**, 4222–4233 (2010).
16. J. Holocher, F. Peeters, W. Aeschbach-Hertig, W. Kinzelbach, R. Kipfer, Kinetic model of gas bubble dissolution in groundwater and its implications for the dissolved gas composition. *Environ. Sci. Technol.* **37**, 1337–1343 (2003).
17. T. Dutta *et al*., Vadose zone oxygen (O2) dynamics during drying and wetting cycles: An artificial recharge laboratory experiment. *J. Hydrol. (Amst.)* **527**, 151–159 (2015).
18. J. O. Helland, E. Jettestuen, Mechanisms for trapping and mobilization of residual fluids during capillary-dominated three-phase flow in porous rock. *Water Resour. Res.* **52**, 5376–5392 (2016).
19. K. Singh, M. Jung, M. Brinkmann, R. Seemann, Capillary-Dominated fluid displacement in porous media. *Annu. Rev. Fluid Mech.* **51**, 429–449 (2019).
20. W. G. Gray, C. T. Miller, TCAT analysis of capillary pressure in non-equilibrium, two-fluid-phase, porous medium systems. *Adv. Water Resour.* **34**, 770–778 (2011).
21. S. M. Hassanizadeh, W. G. Gray, Thermodynamic basis of capillary pressure in porous media. *Water Resour. Res.* **29**, 3389–3405 (1993).
22. J. Niessner, S. M. Hassanizadeh, A model for two-phase flow in porous media including fluid-fluid interfacial area. *Water Resour. Res.* **44** (2008).
23. G. L. Bloomsburg, A. T. Corey, "Diffusion of entrapped air from porous media," PhD dissertation, Colorado State University, Fort Collins, CO (1964).
24. S. Schlüter *et al*., Pore-scale displacement mechanisms as a source of hysteresis for two-phase flow in porous media. *Water Resour. Res.* **52**, 2194–2205 (2016).
25. C. Garing, J. A. de Chalendar, M. Voltolini, J. B. Ajo-Franklin, S. M. Benson, Pore-scale capillary pressure analysis using multi-scale X-ray micromotography. *Adv. Water Resour.* **104**, 223–241 (2017).
26. J. E. McClure, M. A. Berrill, W. G. Gray, C. T. Miller, Influence of phase connectivity on the relationship among capillary pressure, fluid saturation, and interfacial area in two-fluid-phase porous medium systems. *Phys. Rev. E* **94**, 033102 (2016).
27. Y. Hu, Y. She, A. Patmonoaji, C. Zhang, T. Suekane, Effect of capillary number on morphological characterizations of trapped gas bubbles: Study by using micro-tomography. *Int. J. Heat Mass Transfer* **163**, 120508 (2020).
28. R. T. Armstrong *et al*., Porous media characterization using Minkowski functionals: Theories, applications and future directions. *Transp. Porous Media* **130**, 305–335 (2018).
29. J. E. McClure, T. Ramstad, Z. Li, R. T. Armstrong, S. Berg, Modeling geometric state for fluids in porous media: Evolution of the euler characteristic. *Transp. Porous Media* **133**, 229–250 (2020).
30. A. L. Herring *et al*., Effect of fluid topology on residual nonwetting phase trapping: Implications for geologic CO2 sequestration. *Adv. Water Resour.* **62**, 47–58 (2013).
31. L. Andersson, A. Herring, S. Schlüter, D. Wildenschild, Defining a novel pore-body to pore-throat "Morphological Aspect Ratio" that scales with residual non-wetting phase capillary trapping in porous media. *Adv. Water Resour.* **122**, 251–262 (2018).
32. J. A. de Chalendar, C. Garing, S. M. Benson, Pore-scale modelling of Ostwald ripening. *J. Fluid Mech.* **835**, 363–392 (2017).
33. K. Xu, R. Bonnecaze, M. Balhoff, Egalitarianism among bubbles in porous media: An Ostwald ripening derived anticoarsening phenomenon. *Phys. Rev. Lett.* **119**, 264502 (2017).
34. H. Hadwiger, *Vorlesungen über Inhalt, Oberfläche und Isoperimetrie* (Springer, 1957).
35. J. E. McClure *et al*., Geometric state function for two-fluid flow in porous media. *Phys. Rev. Fluids* **3**, 084306 (2018).
36. M. Andrew, B. Bijeljic, M. J. Blunt, Pore-scale contact angle measurements at reservoir conditions using X-ray microtomography. *Adv. Water Resour.* **68**, 24–31 (2014).
37. D. Silin, L. Tomutsa, S. M. Benson, T. W. Patzek, Microtomography and pore-scale modeling of two-phase fluid distribution. *Transp. Porous Media* **86**, 495–515 (2010).

38. S. Iglauer, A. Paluszny, C. H. Pentland, M. J. Blunt, Residual CO2imaged with X-ray micro-tomography. *Geophys. Res. Lett.* **38**, L21403 (2011).
39. M. Andrew, B. Bijeljic, M. J. Blunt, Pore-by-pore capillary pressure measurements using X-ray microtomography at reservoir conditions: Curvature, snap-off, and re-mobilization of residual CO2. *Water Resour. Res.* **50**, 8760–8774 (2014).
40. K. Xu, Y. Mehmani, L. Shang, Q. Xiong, Gravity-induced bubble ripening in porous media and its impact on capillary trapping stability. *Geophys. Res. Lett.* **46**, 13804–13813 (2019).
41. A. L. Herring, L. Andersson, S. Schlüter, A. Sheppard, D. Wildenschild, Efficiently engineering pore-scale processes: The role of force dominance and topology during nonwetting phase trapping in porous media. *Adv. Water Resour.* **79**, 91–102 (2015).
42. R. J. G., Snap-off of Oil droplets in water-wet pores. *Soc. Pet. Eng. J.* **10**, 85–90 (1970).
43. K. Xu *et al*., A 2.5-D glass micromodel for investigation of multi-phase flow in porous media. *Lab Chip* **17**, 640–646 (2017).
44. A. J. Bray, Theory of phase-ordering kinetics. *Adv. Phys.* **43**, 357–459 (1994).
45. Z. Yi *et al*., Pore network extraction from pore space images of various porous media systems. *Water Resour. Res.* **53**, 3424–3445 (2017).
46. T. Ozgumus, M. Mobedi, Effect of pore to throat size ratio on interfacial heat transfer coefficient of porous media. *J. Heat Transfer* **137**, 012602 (2015).
47. G. R. Jerauld, S. J. Salter, The effect of pore-structure on hysteresis in relative permeability and capillary pressure: Pore-level modeling. *Transp. Porous Media* **5**, 103–151 (1990).
48. G. Schnaar, M. L. Brusseau, Pore-scale characterization of organic immiscible-liquid morphology in natural porous media using synchrotron X-ray microtomography. *Environ. Sci. Technol.* **39**, 8403–8410 (2005).
49. D. Stauffer, A. Aharony, *Introduction to Percolation Theory* (CRC Press, London, Boca Raton, ed. 2, 1994).
50. B. Raeesi, M. Piri, The effects of wettability and trapping on relationships between interfacial area, capillary pressure and saturation in porous media: A pore-scale network modeling approach.106 *J. Hydrol. (Amst.)* **376**, 337–352 (2009).
51. A. Patmonoaji, T. Suekane, Investigation of CO 2 dissolution via mass transfer inside a porous medium. *Adv. Water Resour.* **110**, 97–106 (2017).
52. W. B. Haines, Studies in the physical properties of soil. V. The hysteresis effect in capillary properties, and the modes of moisture distribution associated therewith. *J. Agric. Sci.* **20**, 97–116 (2009).
53. F. Moebius, D. Or, Interfacial jumps and pressure bursts during fluid displacement in interacting irregular capillaries. *J. Colloid Interface Sci.* **377**, 406–415 (2012).
54. L. Cueto-Felgueroso, R. Juanes, A discrete-domain description of multiphase flow in porous media: Rugged energy landscapes and the origin of hysteresis. *Geophys. Res. Lett.* **43** (2016).
55. V. Joekar-Niasar, F. Doster, R. T. Armstrong, D. Wildenschild, M. A. Celia, Trapping and hysteresis in two-phase flow in porous media: A pore-network study. *Water Resour. Res.* **49**, 4244–4256 (2013).
56. Y. Edery, S. Berg, D. Weitz, Surfactant variations in porous media localize capillary instabilities during Haines jumps. *Phys. Rev. Lett.* **120**, 028005 (2018).
57. S. Berg *et al*., Determination of critical gas saturation by micro-CT. *Petrophysics* **61**, 133–150 (2020).
58. A. Dalmon, K. Kentheswaran, G. Mialhe, B. Lalanne, S. Tanguy, Fluids-membrane interaction with a full Eulerian approach based on the level set method. *J. Comput. Phys.* **406**, 109171 (2020).
59. M. Grave, J. J. Camata, A. L. G. A. Coutinho, A new convected level-set method for gas bubble dynamics. *Comput. Fluids* **209**, 104667 (2020).
60. C. Xie, A. Q. Raeini, Y. Wang, M. J. Blunt, M. Wang, An improved pore-network model including viscous coupling effects using direct simulation by the lattice Boltzmann method. *Adv. Water Resour.* **100**, 26–34 (2017).
61. A. L. Dye, J. E. McClure, D. Adalsteinsson, C. T. Miller, An adaptive lattice Boltzmann scheme for modeling two-fluid-phase flow in porous medium systems. *Water Resour. Res.* **52**, 2601–2617 (2016).
62. Q. Xiong, T. G. Baychev, A. P. Jivkov, Review of pore network modelling of porous media: Experimental characterisations, network constructions and applications to reactive transport. *J. Contam. Hydrol.* **192**, 101–117 (2016).